



Three-dimensional numerical simulation of dynamic strength and failure mode of a rock mass with cross joints

Tingting Liu^{1,2,3} · Wenxu Huang^{1,2,3} · Chang Xiang^{2,3} · Qian Dong¹ · Xinping Li² · Chao Zhang²

Received: 3 September 2023 / Revised: 9 December 2023 / Accepted: 23 January 2024
© The Author(s) 2024

Abstract

To study the dynamic mechanical properties and failure characteristics of intersecting jointed rock masses with different joint distributions under confining pressure, considering the cross angle α and joint persistence ratio η , a numerical model of the biaxial Hopkinson bar test system was established using the finite element method–discrete-element model coupling method. The validity of the model was verified by comparing and analyzing it in conjunction with laboratory test results. Dynamics-static combined impact tests were conducted on specimens under various conditions to investigate the strength characteristics and patterns of crack initiation and expansion. The study revealed the predominant factors influencing intersecting joints with different angles and penetrations under impact loading. The results show that the peak stress of the specimens decreases first and then increases with the increase of the cross angle. When $\alpha < 60^\circ$, regardless of the value of η , the dynamic stress of the specimens is controlled by the main joint. When $\alpha \geq 60^\circ$, the peak stress borne by the specimens decreases with increasing η . When $\alpha < 60^\circ$, the initiation and propagation of cracks in the cross-jointed specimens are mainly controlled by the main joint, and the final failure surface of the specimens is composed of the main joint and wing cracks. When $\alpha \geq 60^\circ$ or $\eta \geq 0.67$, the secondary joint guides the expansion of the wing cracks, and multiple failure surfaces composed of main and secondary joints, wing cracks, and co-planar cracks are formed. Increasing lateral confinement significantly increases the dynamic peak stress able to be borne by the specimens. Under triaxial conditions, the degree of failure of the intersecting jointed specimens is much lower than that under uniaxial and biaxial conditions.

Keywords Cross joints · Joint distribution form · Dynamic failure characteristics · FEM–DEM · BHPB

1 Introduction

Deep rock mass often forms staggered complex structural planes during tectonic movement. As the most common form of joint in a natural rock mass, cross joints exert a significant influence on the strength and deformation characteristics of a rock mass. In rock engineering practices, such as rock slope protection, tunnel construction, mining engineering, underground powerhouse construction, etc., stability assessment and support design of jointed rock masses

is an important task (Feng et al. 2022; Li et al. 2022). At the same time, in the construction of underground engineering works (Meng et al. 2016; Chen et al. 2023), mechanical vibration or blasting will induce dynamic disturbances of the rock mass. The prerequisite for ensuring the smooth progress of these efforts is the understanding of the mechanical behavior of joints under dynamic loading, especially the mechanical behavior of joints with chaotic and disorderly scales and distribution patterns in nature. In natural rock masses, many joints occur at different scales, and they often intersect (Chang et al. 2019; He et al. 2022). At this time, the deep rock mass bears the dual effects of high ground stress and dynamic disturbance, sometimes leading to engineering disasters such as rockburst or rock mass collapse. Therefore, studying the deformation and strength characteristics of intersecting fractures under the condition of considering the initial damage can provide the most realistic and effective theoretical basis for the stability research of underground engineering in deep complex fractured jointed rock mass. In

✉ Qian Dong
dongqian@jhun.edu.cn

¹ Hubei Key Laboratory of Blasting Engineering, Jiangnan University, Wuhan 430056, China

² School of Civil Engineering and Architecture, Wuhan University of Technology, Wuhan 430070, China

³ Hainan Institute, Wuhan University of Technology, Sanya 572025, China

recent years, many scholars have investigated the mechanical properties of rock mass with cross fractures from the static point of view. Liu et al. (2019) conducted biaxial compression tests on the gypsum time of T-shaped and X-shaped cross joints, and the results showed that with the increase of confining pressure, the failure modes of the samples were surface spalling and lateral cracking; Liu et al. (2017) used a three-dimensional particle flow program to study the influences of geometric parameters on the uniaxial compressive strength of jointed rock mass, and found that the interaction between cross-jointed groups has a significant impact on mechanical properties and failure modes. Zhou et al. (2018) studied the failure mode of two three-dimensional prefabricated cross-cracks in polymethyl methacrylate samples under uniaxial compression. Kulatilake et al. (2001) used the PFC3D program to simulate uniaxial tests on rock masses with cross joints, and found that tensile splitting, slip and composite fracture were the main failure modes of rock masses with cross joints. Xiong et al. (2020) studied the influences of joint parameters such as the inclination angle of the primary joint and the angle between the primary and secondary joint surfaces on the mechanical properties of the specimen. Based on experiments and numerical simulations, Cao et al. (2015) found that such specimens exhibited four failure modes under different inclination angles and included angles.

To ascertain the mechanical properties of intact rocks and fractured rocks under dynamic and static combined loading, scholars have conducted a series of corresponding studies (Hu et al. 2020; Liu et al. 2020, 2019). The dynamic response of the rock under the axial stress state was studied, and the stress–strain curves in the *X*, *Y*, and *Z*-axes were plotted; Li et al. (2008, 2010), based on the dynamic and static combined loading SHPB device, investigated the mechanical properties, energy dissipation, and failure mode of rock specimens under different combined loading conditions; Wang et al. (2018) studied the mechanical properties of coal samples with different water contents under static and dynamic and static combined loads by using a split Hopkinson pressure bar (SHPB) test system; Gong et al. (2012a; b) researched mechanical properties of sandstone under three-dimensional dynamic and static combined loading through the modified triaxial SHPB experimental device, and found that under the same confining pressure, the axial pressure ratio has a greater effect on the compressive strength of sandstone; Xu et al. (2019) studied the dynamic compression performance of concrete specimens under different static triaxial constraints, and found that the specimens exhibited constraint dependence and strain rate dependence; Weng et al. (2018) studied the failure behavior of a rock mass under high ground-stress conditions and

dynamic loads through the SHPB testing of granite rock samples containing circular and cubic holes; based on the improved SHPB device, with the help of three-dimensional digital image correlation technology, Li et al. (2021, 2022) studied the mechanical properties and failure behavior of rocks with fractures under different loading methods; Li et al. (2016) conducted a one-dimensional dynamic and static combined load tests on sandstone specimens with prefabricated holes, and the results showed that the combined effect of stress concentration around the holes and strain generated by static loads promoted rock impact damage; Wang et al. (2022) found that with the increases of the medium thickness and water content, the blocking effect of joints on stress waves was significantly enhanced; Li and Ma (2009) conducted impact tests on rocks containing joints, and found that higher water content and larger joint width would weaken the sample; Li et al. (2018) used the improved SHPB device to perform impact tests on samples containing single joints, and determined six typical crack types therein; Zhang et al. (2006) studied the penetration mechanism of cracks at different spatial positions, and found that cracks easily penetrate directly at the inner ends of the two cracks under dynamic load; Bahaaddini et al. (2016) used the discrete element particle flow program PFC3D to study the influences of the geometric parameters of non-penetrating joints on the uniaxial compressive strength and deformation modulus, it is found that the joint dip angle and joint persistence degree exert a significant influence on the mechanical properties of rock specimens (the joint dip angle exerting the greatest influence); Pan et al. (2021) conducted impact tests on cement mortar specimens with different joint angles, and found that when the joint angle increased from 0° to 90°, the peak strength of the specimens decreased, then increased.

As mentioned above, it is necessary to conduct further Three-dimensional numerical simulation of dynamic strength and failure mode of cross-jointed rock mass. Most of the existing studies on the dynamic response and failure behavior of jointed rock mass focus on single joints or parallel multi-joints, and rarely consider the influence of *in-situ* stress. Although common in many engineering rock masses, cross joints, in terms of structure, are rarely studied. Therefore, based on laboratory tests, this research established a three-dimensional coupling numerical model of the biaxial Hopkinson bar (BHPB) system, considering factors such as different intersection angles, joint persistence ratios, and initial stress states, explored the dynamic strength characteristics of the samples, and analyzed the dynamic strength characteristics of the samples from the microscopic point of view. In this case, the crack initiation-growth mode of the specimen was used to assess the interaction between primary and secondary joints.

2 Numerical model set-up

2.1 Introduction to laboratory testing

The laboratory testing relied on the use of the BHPB test system (Li et al. 2022), as shown in Fig. 1. The loading system consists of a dynamic impact loading unit and a servo-motor controlled hydraulic loading unit. The dynamic impact loading unit includes an air gun, a cylindrical punch and four elastic rods perpendicular to each other on the same horizontal plane. Both the punch and the elastic rod are made of 60Si2Mn alloy steel, and the elastic mold, with a capacity of about 200 GPa, an elastic wave velocity therein of about 5000 m/s, the length of the punch is 500 mm, the diameter is 40 mm, the lengths of the incident rod and the transmission rod are 2.5 m and 2 m respectively, the length of the two rods in the Y-direction is 2 m, and the cross-section of the four rods measures 50 mm × 50 mm. During the test, the punch in the air gun is driven by high-pressure gas to strike the elastic rod at a certain speed, and the maximum impact speed of the punch can reach 30 m/s.

During the test, the pre-loaded initial static load can be applied evenly through the servo-motor controlled hydraulic cylinders in two directions respectively. After it reaches the target value, the impact air pressure is set, and the punch is launched to hit the incident rod to generate the incident stress wave signal ϵ_{in} . When the wave propagates to the end of the incident rod, the reflected wave signal ϵ_{re} and the transmitted wave signal ϵ_{tr} are generated. Meanwhile, the expansion deformation caused by the Poisson effect in the specimen will cause the output rod to more outwards in the Y-direction, so the rod generates dynamic stress wave signals ϵ_{y1} and ϵ_{y2} both of which are monitored and recorded (Fig. 2). According to the one-dimensional stress wave theory and the assumption of uniformity, the mechanical parameters such as dynamic

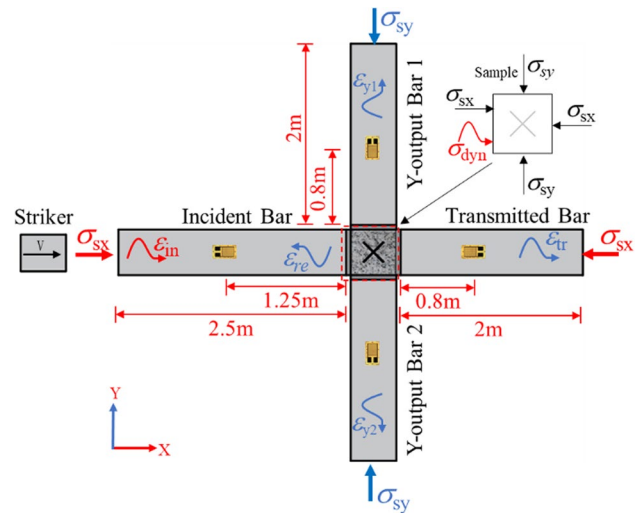


Fig. 2 Plane schematic diagram of the DPHB system (Li et al. 2022; Liu et al. 2023)

stress, dynamic strain, and strain rate in each direction of the specimen were calculated by the three-wave method (Xiao et al. 2020):

$$\left. \begin{aligned} \dot{\epsilon}_x(t) &= \frac{C_0}{L} [\epsilon_{in}(t) - \epsilon_{re}(t) - \epsilon_{tr}(t)] \\ \epsilon_x(t) &= \frac{C_0}{L} \int_0^t [\epsilon_{in}(t) - \epsilon_{re}(t) - \epsilon_{tr}(t)] dt \\ \sigma_x(t) &= \frac{E_0 A_0}{2A_s} [\epsilon_{in}(t) + \epsilon_{re}(t) + \epsilon_{tr}(t)] \\ \epsilon_y(t) &= \frac{C_0}{L} \int_0^t [\epsilon_{y1}(t) + \epsilon_{y2}(t)] dt \\ \sigma_y(t) &= \frac{E_0 A_0}{2A_s} [\epsilon_{y1}(t) + \epsilon_{y2}(t)] \end{aligned} \right\} \quad (1)$$

where C_0 , E_0 , and A_0 are the longitudinal wave velocity, elastic modulus, and cross-sectional area of the rod, respectively;

Fig. 1 The BHPB test system (Li et al. 2022)



A_s and L represent the initial cross-sectional area and length of the sample, respectively; $\epsilon_{in}(t)$, $\epsilon_{re}(t)$, and $\epsilon_{tr}(t)$ denote the incident strain, reflected strain, and transmitted strain in the X -direction, respectively; $\epsilon_{y1}(t)$ and $\epsilon_{y2}(t)$ are the strains in the two output rods in the Y -direction.

The data acquisition system is equipped with a resistance strain gauge (BX120-2AA), an oscilloscope (YOKOGAWA DL-850E), a super-dynamic strain gauge (LK-2019A), a computer and a high-speed data acquisition system. During the experiment, the dynamic voltage signal is amplified by the super-dynamic strain gauge, displayed and cached in real time through the oscilloscope, and then stored for data processing, as shown in Fig. 3a. A high-speed digital image correlation (DIC) measurement system was used to measure the real-time deformation of the sample, and the high-speed camera was vertically placed and aligned with the observation surface of the sample, as shown in Fig. 3b. During the test, when the dynamic voltage signal triggers the oscilloscope, the high-speed camera connected to the oscilloscope

will trigger synchronously, and then start to shoot real-time images. The output results are shown in Fig. 3c.

2.2 Simulation scheme

The test simulates the dynamic response characteristics of samples with different cross-joint distribution forms under two-way confining pressure. The pre-loaded initial static load (σ_{sx} , σ_{sy}) is (30, 10) MPa, and the main joint inclination angle (between the impact loading direction and the joint angle) is 45° , the penetration ω_{L1} is fixed at 0.424, and five different crossing-angle specimens are designed (namely: 30° , 45° , 60° , 90° and 135°); delimiting the range of the joint persistence ratio η as 0.33 to 1.00, the joint width is 0.05 mm. The specimen with a cross angle of 90° and penetration ratio of 0.67 is shown in Fig. 4. The joint persistence ratio η is defined by the ratio of the secondary through joint to the main through joint, as shown in Eq. (2) (Table 1).

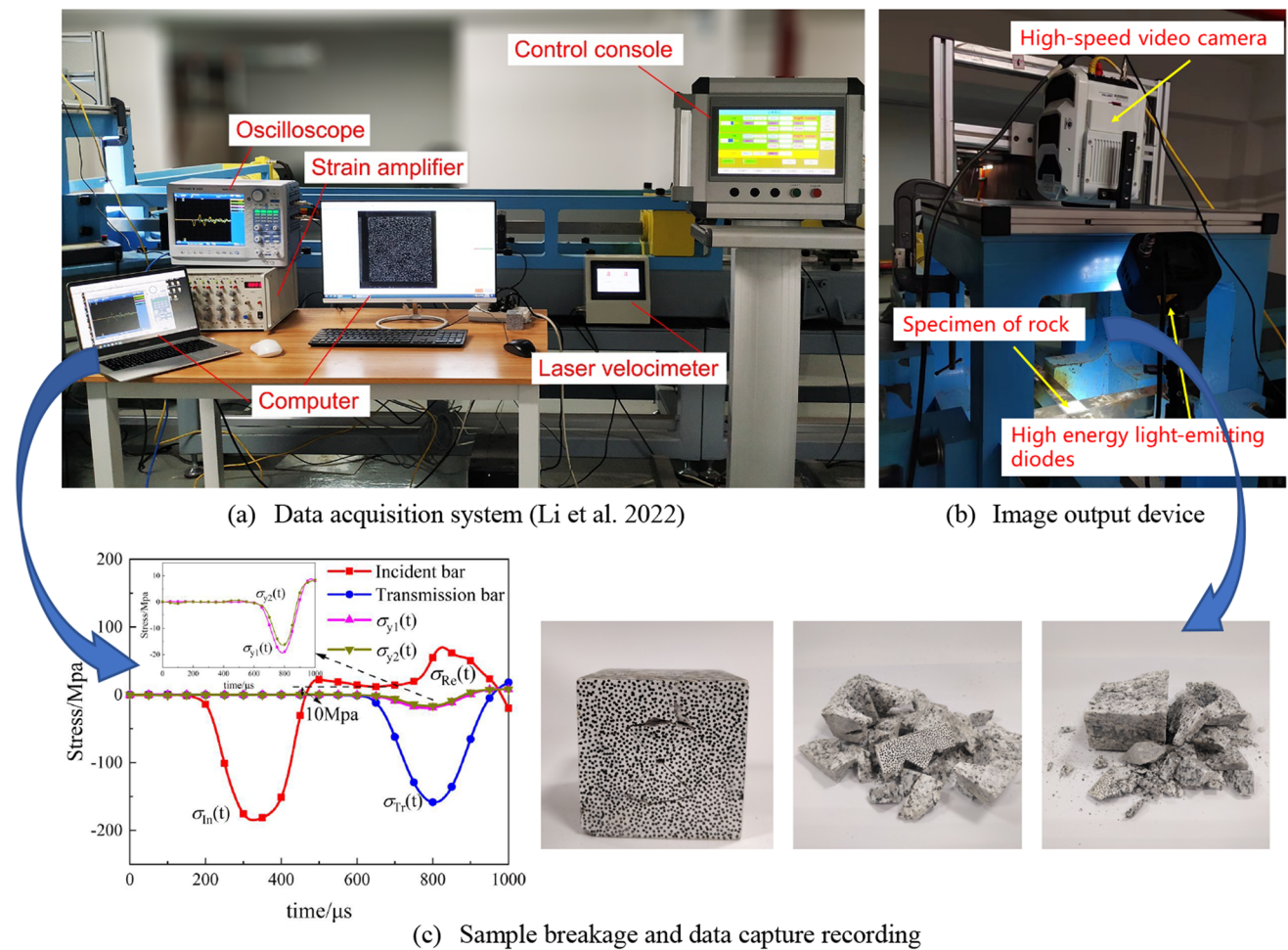


Fig. 3 Laboratory test and result output

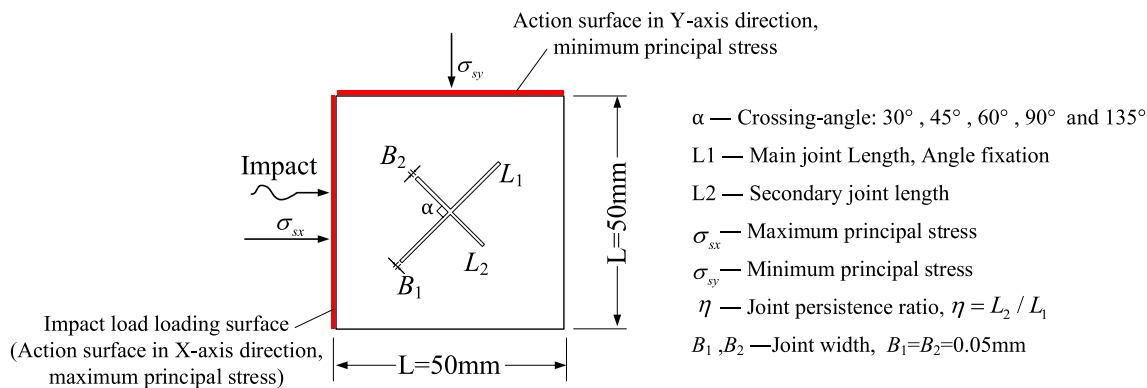


Fig. 4 Schematic diagram of a specimen with a cross angle of 90° and a penetration ratio of 0.67

Table 1 Simulation scheme design

Series No.	Cross angle α (°)	Penetration ratio η
1	30, 45, 60, 90, 135	0.67
2	30, 45, 60, 90	0.33, 0.67, 1.00

$$\eta = \frac{L_2}{L_1} \tag{2}$$

2.3 Construction of numerical model and determination of mesoscopic parameters

Combined with the laboratory test, the same size model of the BHPB system was established by the FEM-DEM coupling method, as shown in Fig. 5a. In this test system, the steel rod is a continuous medium with high yield strength and elastic modulus, in which elastic stress waves can be generated and propagated without attenuation. Therefore, the steel rod is represented by a continuous unit in FLAC^{3D}, while as a rock-soil material, the specimen is represented by the bonded granular material in PFC^{3D}, which is made by deleting particles to form cross joints, and endowed with a “linear parallel bonded contact model (BPM)” (Potyondy 2016) as shown in Fig. 5c. Particles are connected via a linear element and a parallel bond element. Linear elements represented by k_n and k_s can only transmit elastic interactions between particles and cannot resist tension and rotation, and the function of the parallel bond element represented by \bar{k}_n and \bar{k}_s is to bond the particles together (Shi et al. 2019). When the force exceeds the bond strength of the sample, the bond breaks, activating cracking. Force displacement laws for contact force and momentum in the BPM are respectively computed as follows (Cundall and Strack 1979)

$$F_c = F_1 + F_d + \bar{F} \tag{3}$$

$$M_c = M_b \tag{4}$$

where F_1 refers to the linear force, and F_d denotes the hysteretic damping force (Whittaker 1988), which is applied to dissipate energy of the system for each particle in each calculation step; \bar{F} represents the parallel bond force, and M_b stands for the parallel bond moment (Shi et al. 2019).

The coupling wall generated by the “wall-zone” command coincides with the surface of the FLAC solid unit as an interface between the two programs. The coupling wall will be divided into multiple triangular surfaces connected by endpoints. In each cycle, within FLAC^{3D}, the velocity of the boundary node in the model is calculated by the center of gravity interpolation method shown in Fig. 5b through the contact surface node to transfer to the particles in the PFC^{3D} model. The PFC^{3D} model updates the wall coordinates, and then sends the generated wall force back to the FLAC^{3D} model. Therefore, on the boundary of the two models, the coordinates, velocity, and force of will be updated continuously. It is worth noting that during the calculation process, after the coupling option is activated, the mechanical calculation needs to be in the large deformation mode. The Time involved in this numerical calculation is the real time. In the ITASCA business calculation software, the calculation time of FLAC and PDC depends on “Cycle” and “time-step”, and the software uses “Mech-time” to represent the real time. In value, Mech-time = Cycle × time-step, which is different from the running Time in the computer.

In the model building stage, a structural unit with the same size was established as the BHPB test system. The grid size of the steel rod unit was set to 10 mm × 5 mm × 5 mm, and the parameters such as the elastic modulus and Poisson’s ratio of the steel rod were

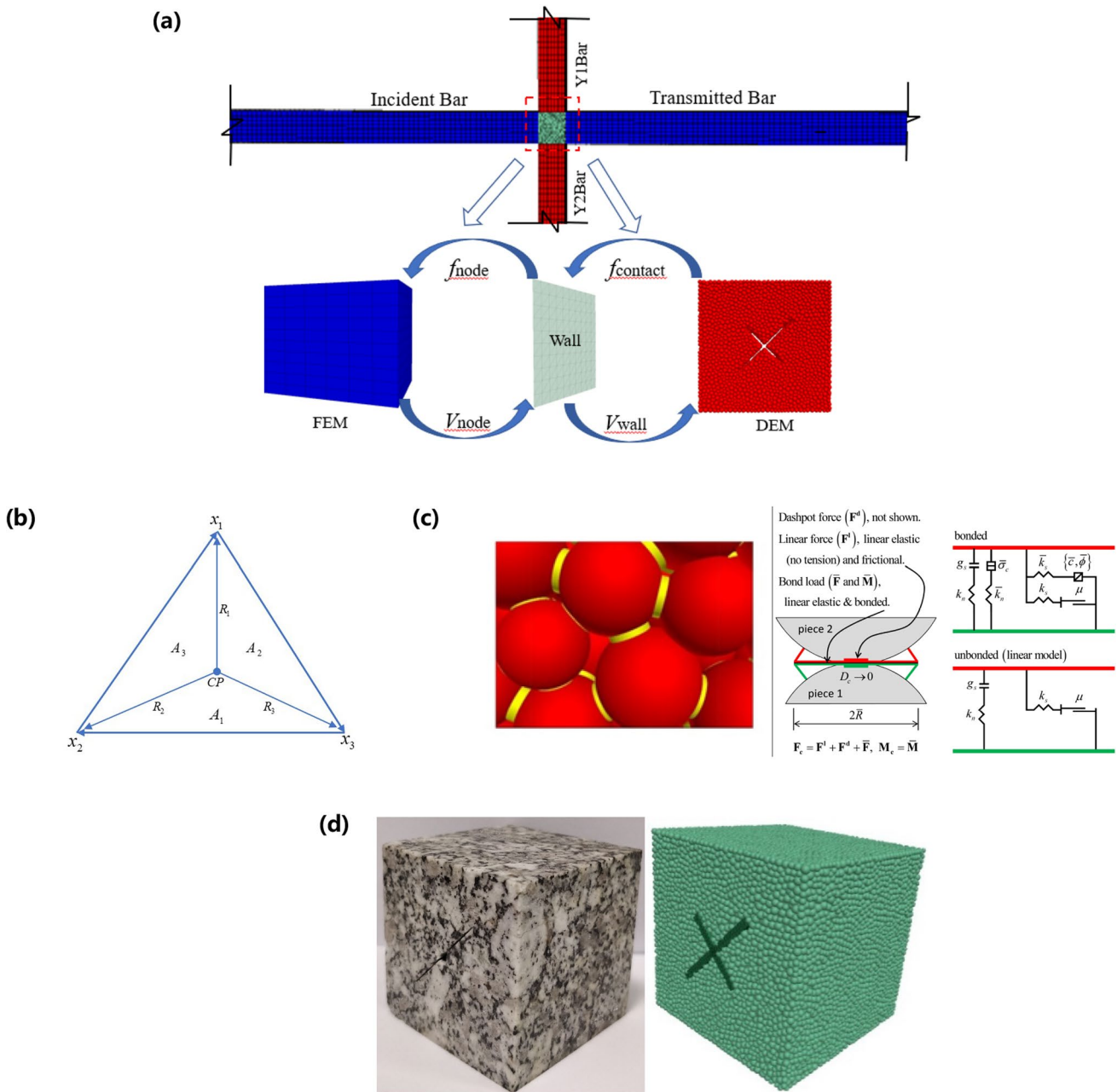


Fig. 5 Schematic diagram of numerical model of the BHPB system. **a** Numerical model (schematic representation) **b** Center of gravity interpolation **c** Linear parallel bonded contact model **d** Cross-jointed specimen

set according to the standard procedure in the friction-free state. A numerical specimen of the same size was generated as the laboratory specimen (50 mm × 50 mm × 50 mm), as shown in Fig. 5d, the minimum diameter D_{min} of the sphere was set to 1.2 mm, the ratio of the maximum diameter D_{max} to D_{min} was set to 1.67, and parameters such as density and damping to the sphere were assigned; in the model test stage, at first, static loads σ_{sx} and σ_{sy} were applied to the rod ends in the X and Y -directions respectively. After the specimen reached the static stress

balance, the dynamic configuration was activated and the local dynamic damping was set to 0. A dynamic load was applied to the left-hand end of the incident rod, and the generated stress wave propagated through the incident rod and strikes the specimen. Part of the stress wave propagated through the specimen to the transmission rod, and part of it propagated to the two rods in the Y -direction due to the Poisson effect in the specimen. The output rod, and the rest can be reflected along the incident rod, completing the propagation of the stress wave.

Table 2 Mesoscopic parameters of the numerical model

Parameter	Value
Density (kg/m ³)	2620
R_{\min} (mm)	0.6
D_{\max}/D_{\min}	1.67
Frictional coefficient μ	0.39
k_{rat}	1.8
Effective modulus (GPa)	25.0
Porosity	0.15

Table 3 Mesoscopic parameters of bond in the numerical model

Parameter	Value
Pb-tension (MPa)	21.0
Pb-cohesion (MPa)	41.0
Stiffness ratio	1.8
Friction angle (°)	40
Installation gap (mm)	0.03

Table 4 Mesoscopic parameters of bar in the numerical model

Parameter	Value
Elastic modulus (GPa)	200
ν	0.27
Wave speed (m/s)	5000
Density (kg/m ³)	78.50

Based on the laboratory test results, the mesoscopic parameters of the numerical model were checked and corrected by trial and error; more reliable numerical simulation mesoscopic parameters were obtained (Tables 2, 3, 4). In this process, besides considering the physical and mechanical parameters of the material itself, the "Pb-tension" and "Pb-cohesion" parameters play a significant role, and accurate calibration of these two parameters is crucial for reproducing the numerical simulation faithfully.

Figure 6 illustrates the comparison between the laboratory BHPB test results and the numerical BHPB test results of the samples. The stress-time history curve of the incident stress wave in the laboratory test, depicted in Fig. 6a, serves as the basis for the numerical simulation input. The impact load applied to the rod end exhibits a remarkable consistency with the incident wave of the test, validating the successful implementation of the stress wave input. Figures 6b–d display the propagation characteristics of the output stress wave, demonstrating a high degree of agreement between the curves obtained from the laboratory test and numerical simulation. Figure 6e showcases the final failure pattern, where the accumulation of light-yellow particles indicates the crack area. These comparisons collectively affirm the reliability and effectiveness of the numerical test model parameters.

3 Simulation result analysis

3.1 Stress equilibrium

The impact test simulation was conducted on specimens with a joint persistence ratio η of 1.0, the initial static load (σ_{sx} , σ_{sy}) is (30, 30) MPa to verify the stress wave propagation and stress balance, the test input impact stress wave is a quasi-half-chord wave, the amplitude of which is about 180 MPa. Multiple monitoring points among the incident rod, transmission rod and Y-direction output rod were set to monitor the stress amplitude. The stress history of each rod is shown in Fig. 7, and the stress amplitude of the monitoring point on the incident rod can be found. The values are the same, indicating that the propagation of the input stress wave in the member is not attenuated. At the same time, to ensure the accuracy of the BHPB simulation test, the specimen must reach a dynamic stress equilibrium during the test.

Figure 8 shows the results of verifying the stress equilibrium through the "three-wave method" and "direct method". In the three-wave method, the transmitted wave is the superposition of the incident wave and the reflected wave; In the direct method, the stress at the interface between the rod and the specimen at both ends (incident and transmitted ends) is equal to the average stress within the specimen after the impact. The stress at the contact interface (incident end $\sigma_{\text{in}}^{\text{surf}}$ and transmission end $\sigma_{\text{tr}}^{\text{surf}}$) is equal to the average stress σ_{ave} in the specimen. Remarkably, the specimen maintains a dynamic stress equilibrium in both scenarios, thereby confirming the validity of the test model.

3.2 Strength characteristics

3.2.1 Effects of cross angle

Figure 9a shows the dynamic stress–strain curves of samples with five cross angles. The stress–strain curves of samples can be divided into three stages: an elastic deformation stage, non-linear deformation stage, and post-peak stage. The difference in the stress–strain curve of the static test on a rock specimen is that under the action of the initial static load, the internal micro-cracks of the specimen are compacted, so no compaction section is observed in the stress–strain curve of the specimen during the impact loading process. In the elastic deformation stage, the compressive deformation of the specimen is uniform, and the dynamic elastic modulus of the samples with different cross-joint angles is relatively consistent; as the dynamic stress continues to increase, the microcracks are activated,

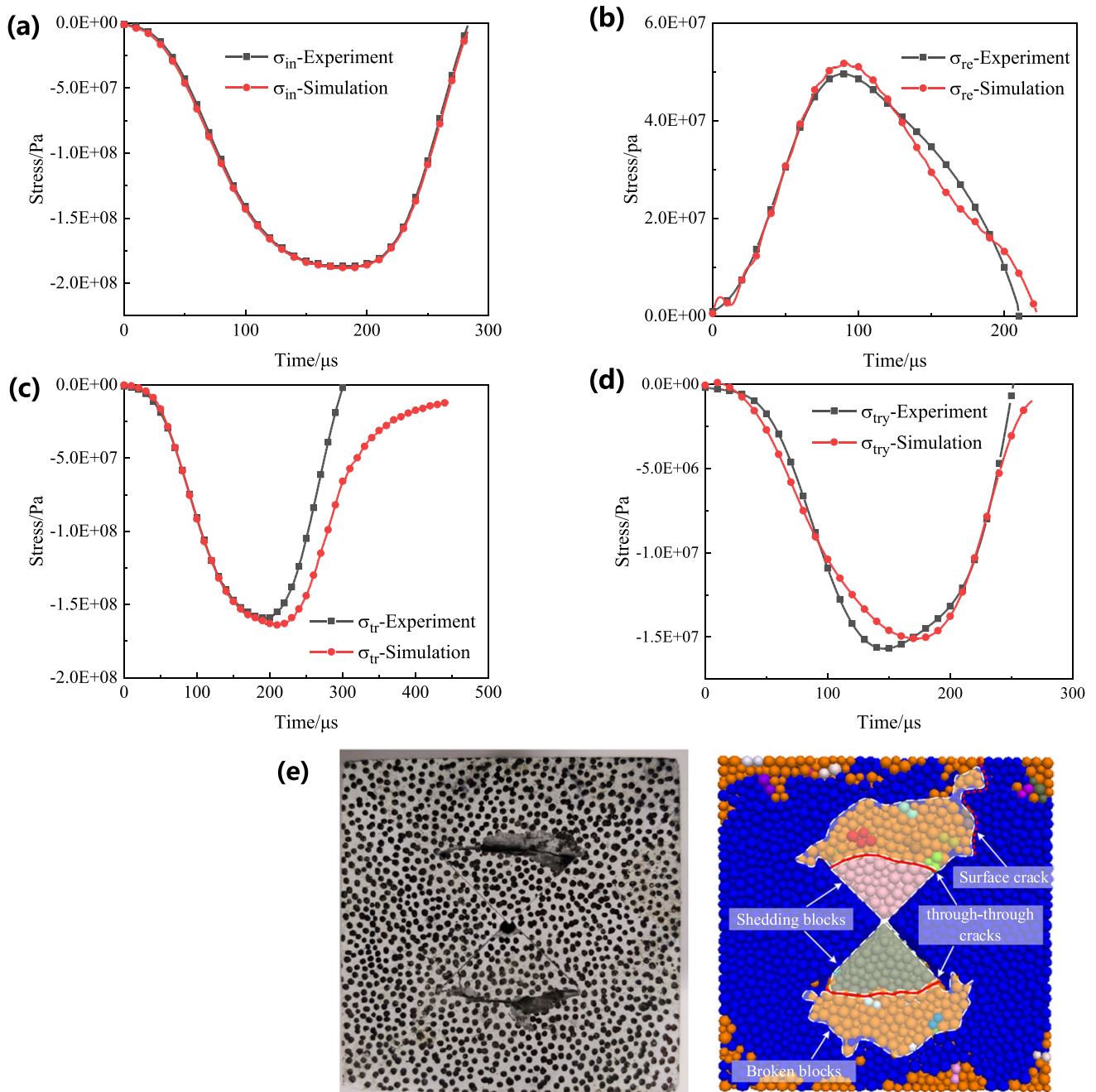


Fig. 6 Comparison of waveforms and final failure forms. **a** Incident waves **b** reflected waves **c** transmission waves **d** transmitted wave in the Y-direction **e** comparison chart of the final failure form of the sample

and the specimen enters the non-linear deformation stage; in the post-peak stage, after the impact load is reduced, the elastic strain energy stored in the specimen is released, but because the specimen is not completely destroyed during the impact process and retains a certain bearing capacity, the stress–strain curve of the specimen rebounds during the unloading stage, forming a hysteresis loop. Figure 9b compares the stress–strain curves of experiment and simulation under a confining pressure of 30 MPa, in which the

test data are obtained through laboratory tests as shown in Fig. 3. The two curves closely coincide, with a peak difference of less than 1.5%, validating the effectiveness of the numerical simulation in this study.

The peak stresses borne by samples with different cross angles are shown in Fig. 10. When the cross angle increases from 30° to 135°, the peak stresses on samples are 171.1, 169.8, 167.8, 163.4, and 164.8 MPa, initially decreasing, then increasing. There is a large change initially, but the

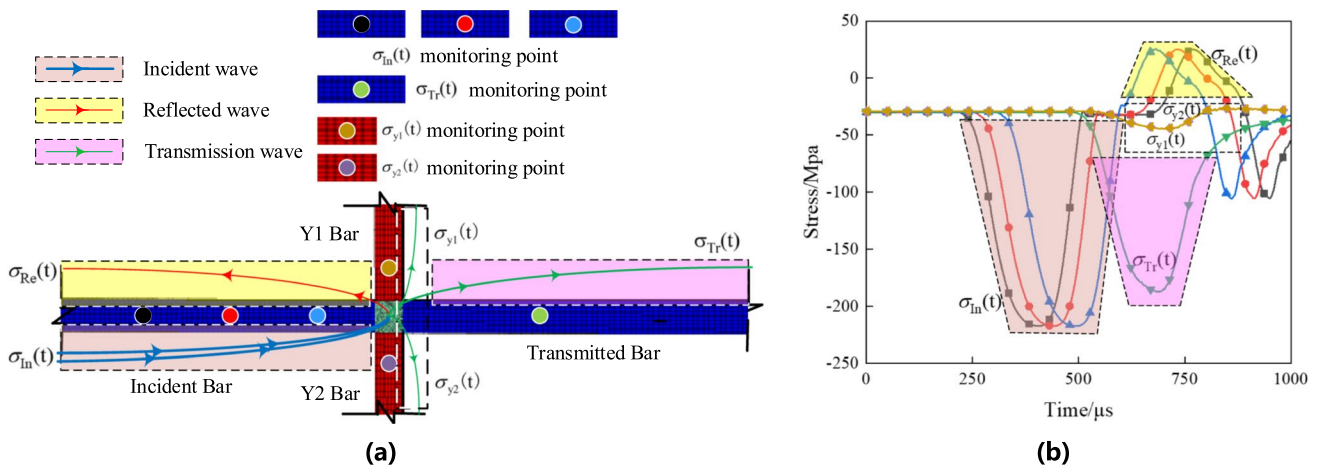


Fig. 7 Laboratory test and monitoring curve. **a** Diagram of stress wave propagation over SHPB **b** stress-time curve

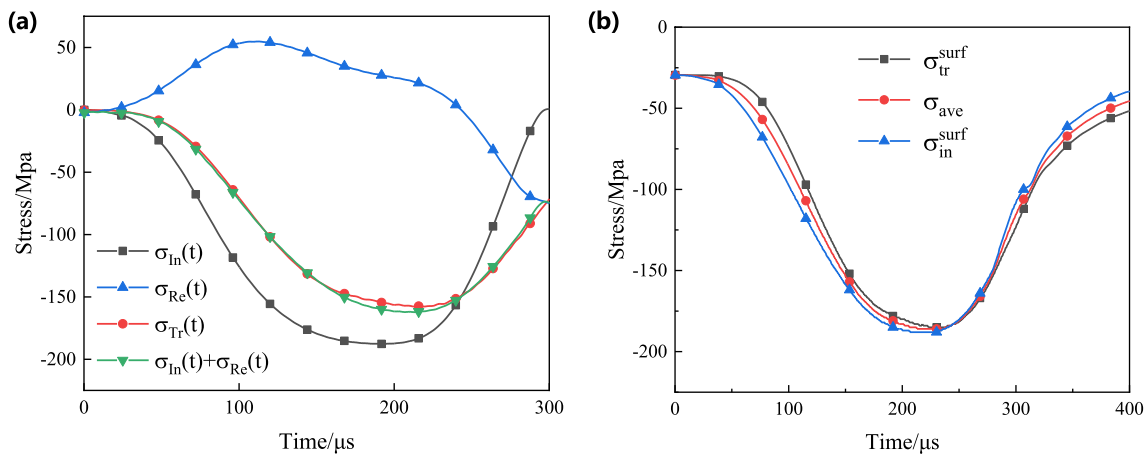


Fig. 8 Dynamic stress equilibrium check. **a** Three-wave method **b** direct method

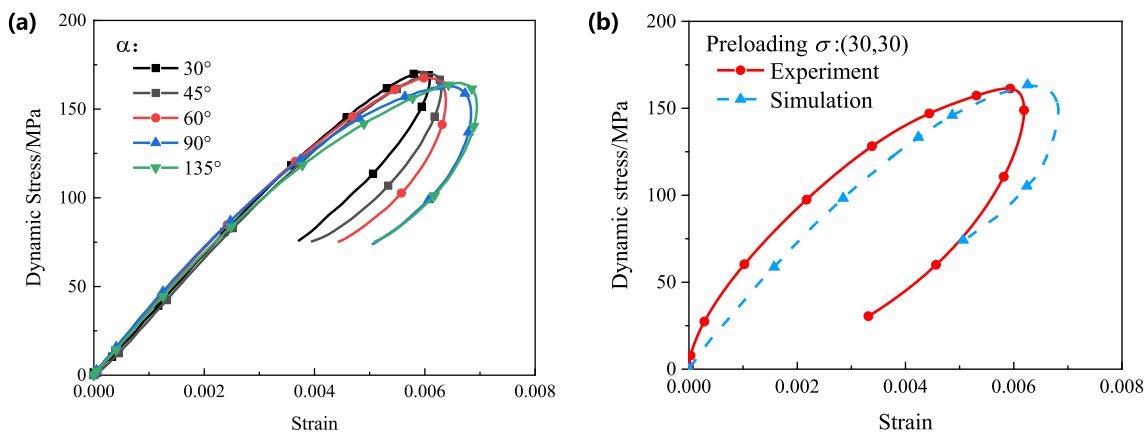


Fig. 9 Stress–strain curves. **a** Stress–strain curves of different cross-jointed specimens **b** comparison of Indoor Testing and Numerical Simulation under a Confining Pressure of 30 MPa (Liu et al. 2023)

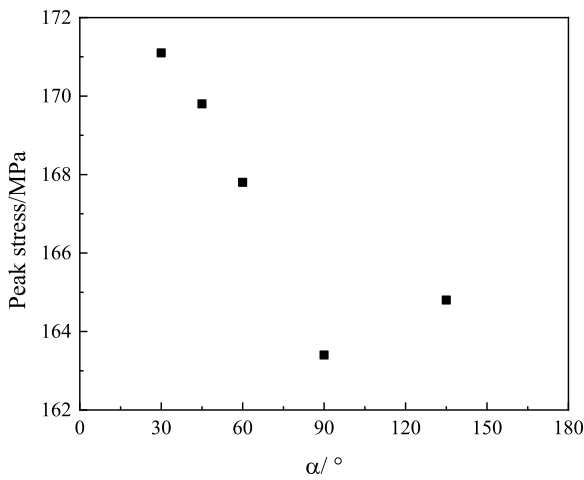


Fig. 10 Peak stress borne by specimens with different cross-joint angles

overall change is small. It is considered that when the length and dip angle of the main joint are constant, the change of the dip angle of the secondary joint has little effect on the strength of the rock sample, and the strength of the

cross-joint specimen is mainly controlled by the main joint. The peak stress of the specimen with an included angle of 90° is the smallest, indicating that when the secondary joint is orthogonal to the main joint, the joint has a significant effect on the deterioration of the strength of the rock sample, thereby reducing the impact resistance of the rock specimen.

3.2.2 Effects of the joint persistence ratio

To study the effect of the joint persistence ratio on the strength characteristics and failure mode of the cross-joint specimens, and according to the laboratory test results, it can be found that when the intersection angle is 90°, there will be through-through cracks formed between the primary and secondary joints of the specimens with different penetration ratios, so respectively dynamic biaxial compression tests were conducted on samples with different penetration ratios at intersection angles of 30°, 45°, 60°, and 90° to assess the influence of the interaction between primary and secondary joints.

Figure 11 shows the stress–strain curves of the samples obtained by processing the data; as the cross angle α increases from 30° to 90°, the peak strain increases, and

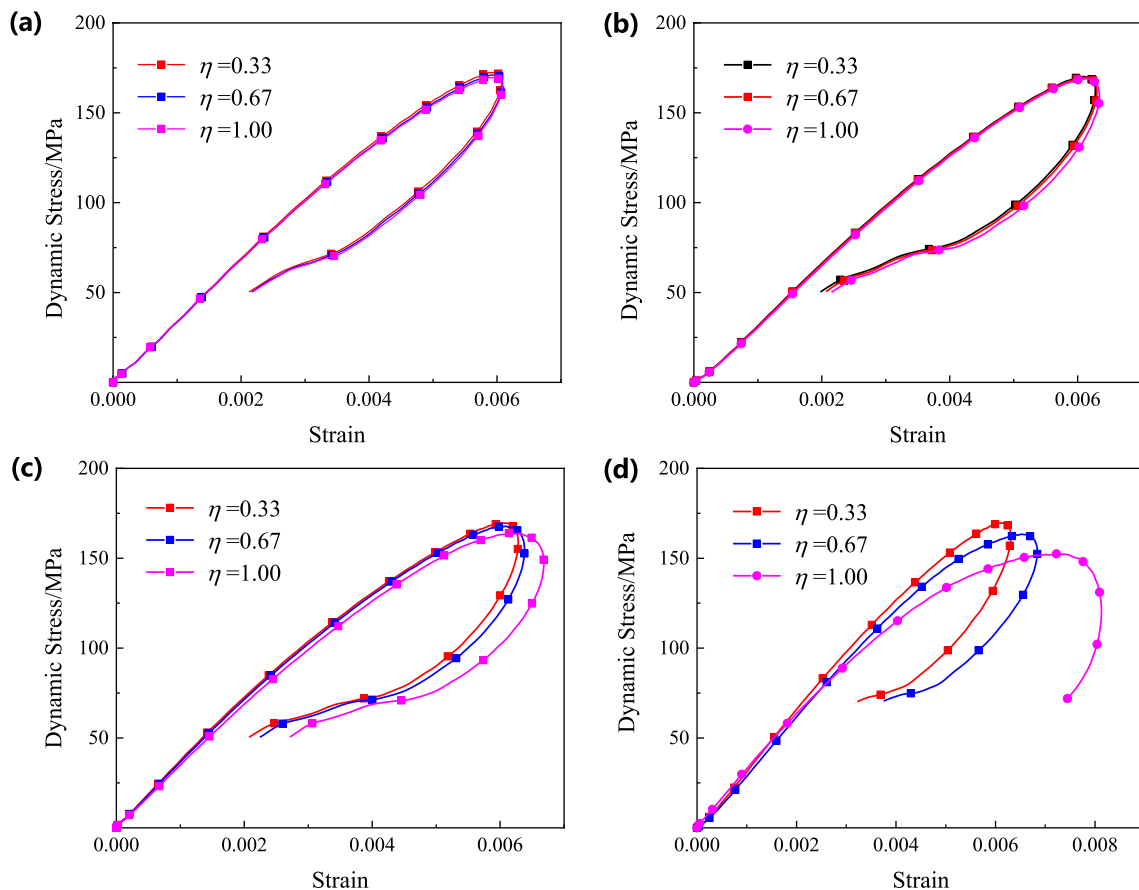


Fig. 11 Stress–strain curves of samples with different penetration ratios at different cross angles. **a** $\alpha = 30^\circ$ **b** $\alpha = 45^\circ$ **c** $\alpha = 60^\circ$ **d** $\alpha = 90^\circ$

Table 5 Confining pressure setting

Test type	σ_{sx} (MPa)	σ_{sy} (MPa)	σ_{sz} (MPa)	Abbreviation
Uniaxial compression test (UC)	0	0	0	(0, 0, 0)
Biaxial compression test (BC)	30	20	0	(30, 20, 0)
True triaxial compression test (TC)	30	20	10	(30, 20, 10)

the hysteresis loop in the post-peak stage also increases. Large, that is, the elastic strain energy released in the specimen increases, and the degree of damage to the specimen increases, indicating that regardless of the joint persistence ratio, the increase of the cross angle will reduce the ability of the specimen to resist damage, which is consistent with the aforementioned conclusion. When the intersection angle α is 30° and 45° , the dynamic peak stress of the specimen changes little with the joint persistence ratio η , which indicates that the strength of the specimen is controlled by the main joints, and the increase in the length of the secondary joints has almost no effect thereon. When the intersection angle α is 60° , the peak stress decreases slightly with increasing η , and when α is 90° , the peak stress decreases from 169.7 MPa to 152.4 MPa with the increase of η from 0.33 to 1.00. The strain also decreased significantly, indicating that when $\alpha \geq 60^\circ$, the sub-joint began to affect the dynamic strength of the sample, and for the 90° -specimen with the lowest strength, the influence of the length of the sub-joint is more significant. The initial deterioration effect on the specimen is superimposed, so the dynamic strength decreases significantly.

From the above analysis, when $\alpha < 60^\circ$, the peak strength of specimens from different angles is essentially the same, and the hysteresis curves of specimens with different joint persistence ratio at the same angle overlap significantly. the dynamic strength of the specimen is controlled by the main joints; when $\alpha \geq 60^\circ$, the primary and secondary joints exert the more significant effect on the strength: the trend of hysteresis curve shows that secondary joints can better determine the peak strength; at $\alpha = 90^\circ$, the length of secondary joints has a significant effect on the strength.

3.2.3 Effects of the initial stress state

The above simulation results found that the strength of the specimen is low when the cross angle is 90° under biaxial compression, and the interaction between the primary and secondary joints is manifest to a significant extent when the penetration ratio is 0.67. To understand the influence of the dynamic strength of the sample, impact simulation tests under uniaxial, biaxial and triaxial stress states (as shown in Table 5) were conducted on specimens with $\alpha = 90^\circ$ and $\eta = 0.67$, respectively. Figure 12 shows a numerical model of a specimen under a triaxial state of stress. In the context of this discussion, "uniaxial" means that there is no lateral

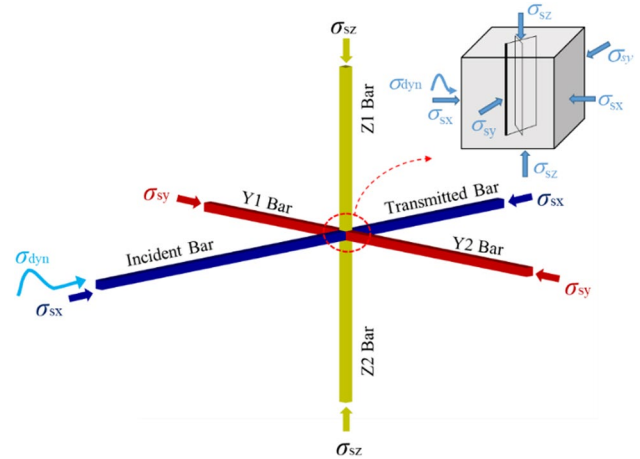


Fig. 12 Numerical model of a specimen under a triaxial state of state

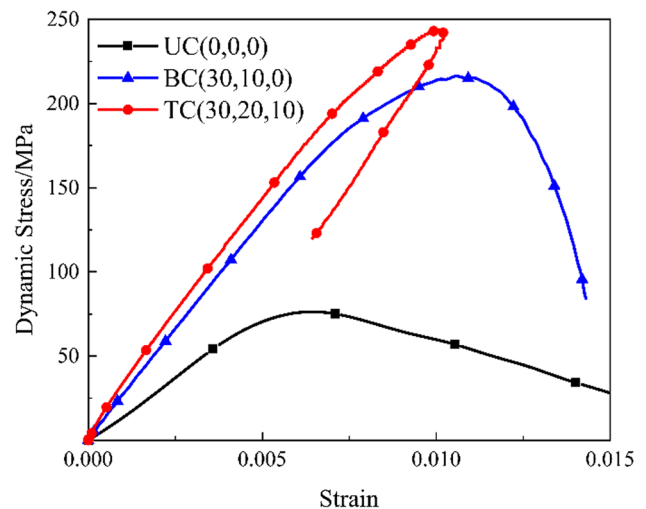


Fig. 13 Test results under multiaxial prestressing

pressure, and only the impact load is applied in the specified direction, denoted as UC (0, 0, 0). Similarly, "Biaxial loading" is expressed as BC (30, 10, 0), and the "triaxial loading" is expressed as TC (30, 20, 10).

Figure 13 depicts the stress–strain curves of the specimen in the multiaxial prestressed state. Since in the numerical simulation, the cross-joint specimen is in a quasi-compacted state after sampling; under uniaxial compression, the stress–strain curve of the specimen does not exhibit a

compaction stage, and directly enters the elastic deformation stage. Under uniaxial and biaxial compression, the specimen exhibited strain softening in the post-peak stage, increased plastic deformation, and the stress–strain curve was open in form. Under triaxial compression, the specimen still retains its strength, and the stress–strain curve rebounds in the post-peak stage, forming a hysteresis loop.

Figure 13 shows that with the strengthening of lateral constraints, the dynamic strength and dynamic elastic modulus of the specimen increase significantly, and its peak stress increases from 76.3 MPa under uniaxial compression to 244.2 MPa (triaxial compression), this shows that the increase of lateral restraint can significantly improve the dynamic strength of the specimen. In Fig. 13, UC, BC and TC represent uniaxial compression, biaxial compression and triaxial compression respectively.

3.3 Failure mode of specimens at different cross angles

According to previous studies on the evolution process of rock damage, the damage of rock is essentially the result of the continuous initiation, expansion, and accumulation of micro-cracks in the rock mass, therefore, the damage evolution process of the rock specimen can be analyzed by observing the microcrack propagation process in the numerical simulation. The red stripes in Table 5 represent microcrack sheets that originate and propagate from the tip of the joint. As the impact load increases, the crack density also increases, resulting in the formation of a macroscopic crack zone known as the damaged and fractured zone. On the other hand, the different colors depicted in Fig. 13 represent various rock states.

When the cross angle is 30° , after the stress wave reaches the specimen (at $540 \mu\text{s}$), due to the influences of preloaded static load and impact force, stress concentration will appear on the contact edge between the steel rod and the sample, so the stress concentration will appear on the edge of the specimen and randomly distributed microcracks will be generated at the corner; wing cracks and anti-wing cracks will then be generated quasi-simultaneously at the tip of the main joints. However, due to the bidirectional static load, the wing cracks are limited in the extent of their propagation and appear as thin microcrack sheets on a microscopic scale. With the increase of impact load, between $650 \mu\text{s}$ and $1000 \mu\text{s}$, the anti-wing cracks continue to expand from the tip of the main joint to the end of the sample, and the coplanar cracks are discretely generated in the area between the main joint and the end of the sample, and the crack density increases with the increase of the impact load. As the width and length continue to increase, the local area where the cracks gather also increases and is separated from the rest of the area. The expansion, intersection, aggregation, and penetration of

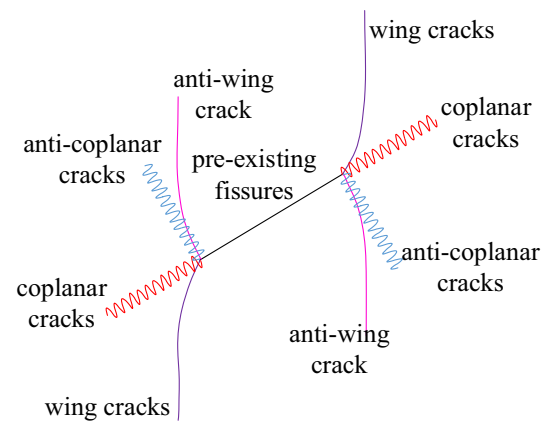


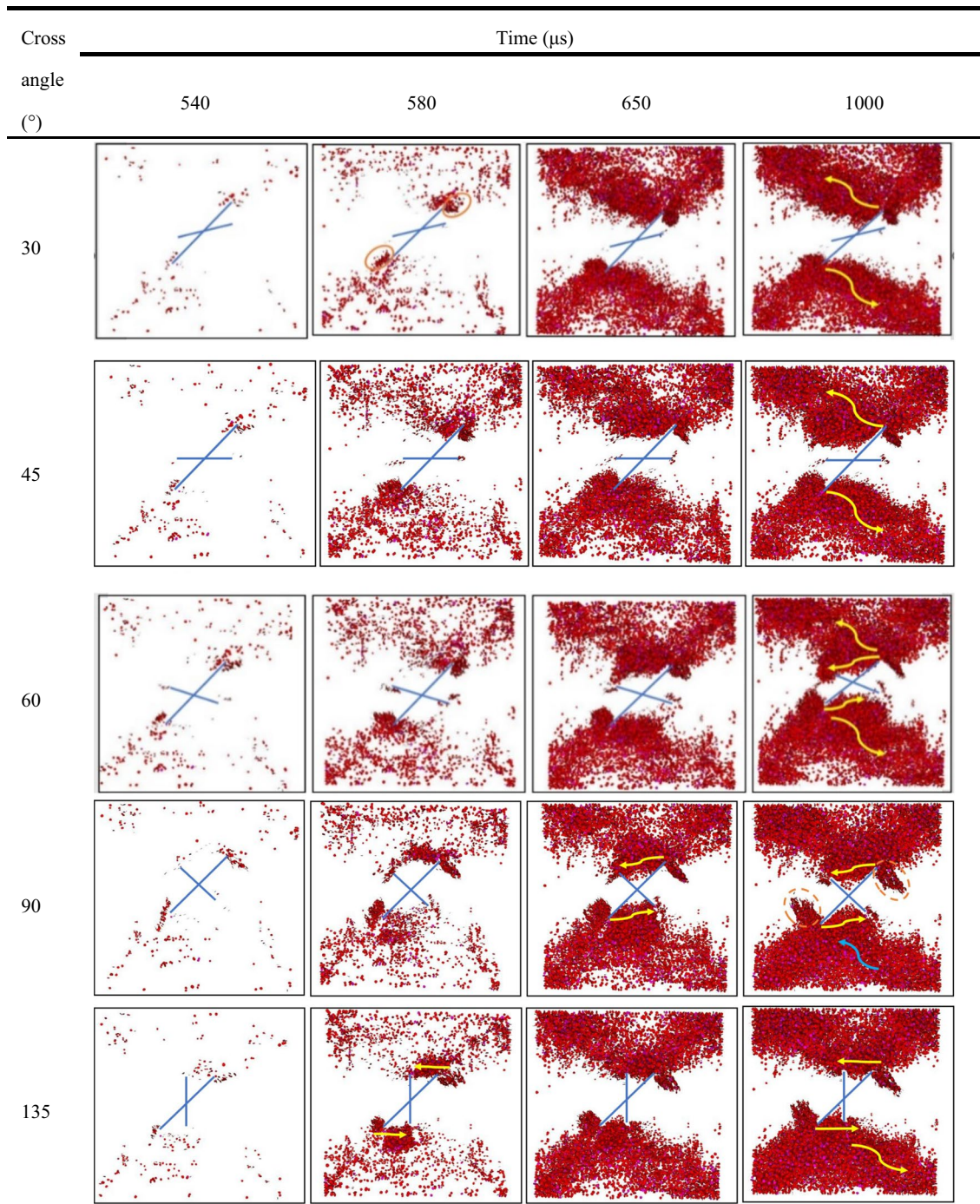
Fig. 14 Schematic diagram of crack initiation types (Liu et al. 2015)

these cracks cause the rupture of the specimen. From a mesoscopic point of view, the anti-wing cracks at the upper and lower ends of the specimen show an antisymmetric propagation trend at an angle of approximately 135° to the loading direction, and finally penetrate through the end of the specimen. During the destruction of the sample, the cracks are generated and propagated from the tip of the main joints, and the secondary joints have almost no influence on the crack-propagation path. In this numerical simulation study, the observed form of cracks is depicted in Fig. 14.

The final failure form of the crack propagation path of the specimen with an intersection angle of 45° is like that of the 30° -specimen, and the wing cracks initiate and propagate approximately perpendicular to the main joints. Between $650 \mu\text{s}$ and $1000 \mu\text{s}$, the impact load increases, and the microcracks appear along the main joints. The tip tends to expand downwards and upwards respectively around the main joints. During the impact process, the main joints dominate the failure process of the sample, and the secondary joints still have little influence on the crack propagation path. The interaction between the primary and secondary joints is not obvious. The specimen eventually exhibited shear failure.

The crack propagation process of the specimen with a cross angle of 60° is shown in Table 6. The red particles in the output result indicate the microcrack, and the arrows drawn show the direction of the crack propagation. At $580 \mu\text{s}$, the anti-wing crack tends to propagate from the tip of the main joint along the direction of the maximum principal stress. At $650 \mu\text{s}$, the crack density at the corner end of the specimen gradually increases, the anti-wing cracks penetrate at the tip of the primary and secondary joints, and coplanar cracks are generated at the lower end of the main joints. As the impact load increases, the coplanar cracks and anti-wing cracks continue to expand and coalesce, and finally the cracks at penetrate the end of the specimen, and the multiple fracture surfaces consisting of anti-wing cracks,

Table 6 Crack growth in specimens with different cross angles



primary joints, secondary joints, and coplanar cracks are formed within the specimen.

At the initial loading stage of the specimen with a cross angle of 90°, tensile wing cracks were initiated at the tips of the primary and secondary joints. At 580 μs, the anti-wing cracks tended to penetrate at (or around) the primary and secondary tips, and the wing cracks continued to expand, the anti-wing crack completely penetrates at the tip of the

primary and secondary joints, and continues to expand to both ends of the specimen through the end of the primary joint, resulting in macroscopic fracture of the specimen.

The crack propagation process of the specimen with a cross angle of 135° is similar to that of the 90°-sample, but the wing crack length is significantly longer than other samples, and the ends of the primary and secondary joints penetrate within a short period of time, and after penetration,

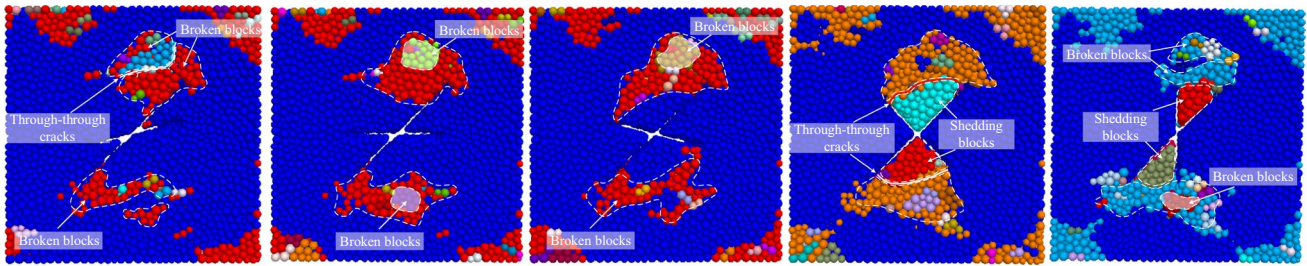


Fig. 15 Final failure patterns of specimens with different cross-joints

the crack passes through (causing expansion of the end of the secondary joint) to the two ends of the sample, the joint action of the two joints leads to the destruction of the specimen. Figure 15 presents the final failure morphology of the specimens at each cross angle. The interface between balls of different colors signifies the occurrence of crack penetration.

From the above analysis, there are differences in the failure characteristics of samples with different cross angles. When the cross angle α is less than 60° , the cracks in the specimen mainly propagate from the main joints, and the secondary joints have little influence on the crack propagation path. When $\alpha \geq 60^\circ$, the secondary joints have a guiding effect on the propagation of the anti-wing cracks, and there will be significant penetration failure between the primary and secondary joints. Joint control, and the formation of multiple fracture surfaces composed of anti-wing cracks, primary and secondary joints, and coplanar cracks (the specimen is more damaged).

3.4 Failure modes of samples with different penetration ratios

Table 7 summarizes the final failure modes of samples with different penetration ratios at different intersection angles: when the intersection angle α is 30° and 45° , the crack initiation and propagation are dominated by the main joints, regardless of the joint persistence ratio η ; the size (the length of the sub-joint) has no significant effect on the crack initiation-propagation process, which corresponds to the influence of the joint persistence ratio on the strength characteristics at this angle above. When the intersection angle α is 60° , and when η is 0.33, the secondary joints of the specimen have little effect on its failure mode; when $\eta \geq 0.33$, secondary joints exert a guiding effect on crack propagation, and penetration failure occurs between the ends of the primary and secondary joints.

In summary, when the intersection angle $\alpha < 60^\circ$, the primary joints dominate the crack initiation and propagation, and the secondary joints have little effect on the strength and failure mode of the rock specimen. When $\alpha \geq 60^\circ$, the

crack initiation and expansion remain dominated by the main joints, but the influence of the secondary joints on the crack growth gradually increases. Combining the failure characteristics of samples with different intersection angles and penetration ratios, it is considered that, under this loading condition (when $\alpha = 60^\circ$, $\eta = 0.67$ and the length of the secondary joint is 20 mm) the critical condition for the interaction between the primary and secondary joints arises. The distribution of stress fields near the ends of primary and secondary joints overlaps. When $\alpha \geq 60^\circ$ and $\eta \geq 0.67$, the size of η will affect the time required for the formation of cracks at the ends of primary and secondary joints. When $\alpha < 60^\circ$, regardless of the size of η , there will be no penetrating failure between primary and secondary joints.

3.5 Failure modes of specimens under different initial stress states

Figure 16 demonstrates the crack growth process of the specimen under uniaxial compression. The cracks in the specimen are mainly wing cracks and coplanar cracks, which is different from the situation in the presence of static stresses alone. At the initial stage of loading, wing cracks are generated at the tips of the primary and secondary joints. At about $680 \mu\text{s}$, the right-hand wing cracks are connected near the right-hand tips of the primary and secondary joints, and coplanar cracks are initiated at the lower tips of the main joints and propagate toward the lower end of the specimen. At $740 \mu\text{s}$, coplanar cracks are generated at the tip of the main joints and propagate through the upper end of the sample, but between $740 \mu\text{s}$ and $1000 \mu\text{s}$, generation of micro-cracks diminishes, and the final failure mode of the specimen is “tensile-shear composite”. Combining the failure pattern of the specimen as shown in Fig. 17, it is found that the specimen is separated by the crack zone and the fracture surface composed of the main joints, and completely loses its bearing capacity. This shows that, under the lower impact load, the specimen will be destroyed macroscopically, so as the impact load continues to increase, the micro-cracks inside the specimen will not continue to increase.

Table 7 Final failure patterns of samples with different penetration ratios at different intersection angles

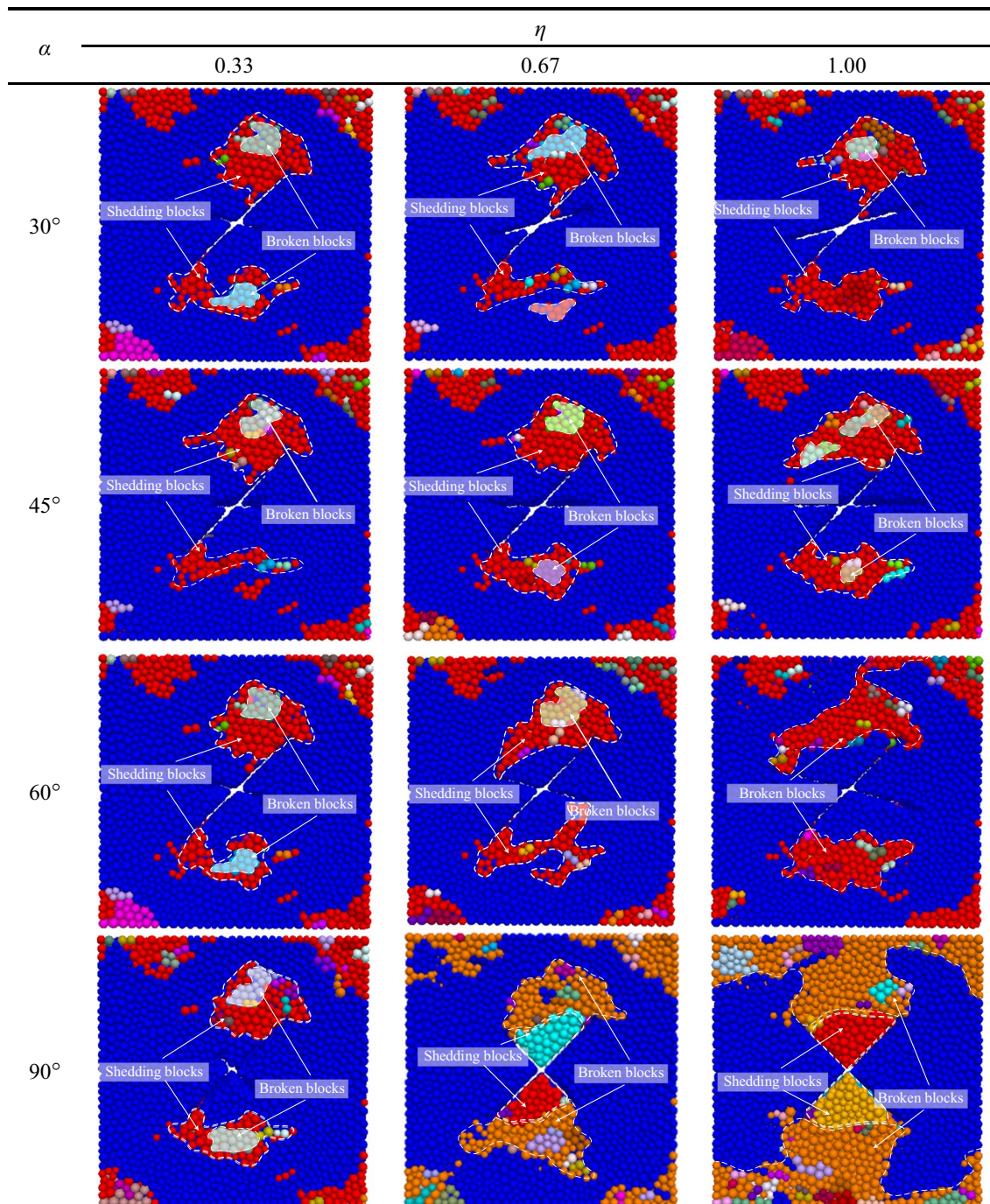


Figure 18 shows the failure morphology of the specimens under biaxial and triaxial compression. It can be found that under biaxial compression, the crack density in the area between the tip of the primary and secondary joints and the end of the specimen increases in the later stage of loading, while the degree of damage in the specimen under triaxial compression is significantly lower than that of biaxial

compression, which also shows that the lateral The increase of constraints can suppress the generation of microcracks to a certain extent and improve the impact resistance of the specimen.

In summary, under uniaxial compression, wing cracks and coplanar cracks are the dominant cracks; under load, a penetrating fracture zone composed of main joints and crack zones

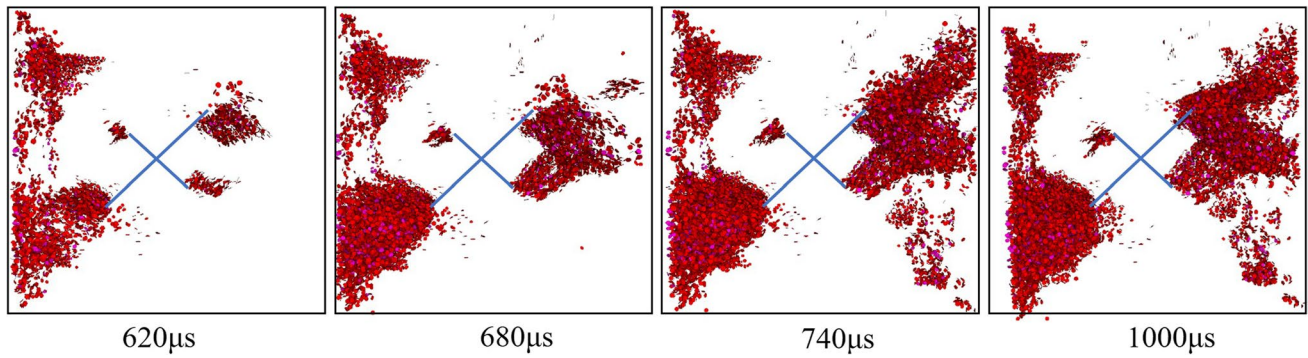


Fig. 16 Crack growth in a specimen under uniaxial compression

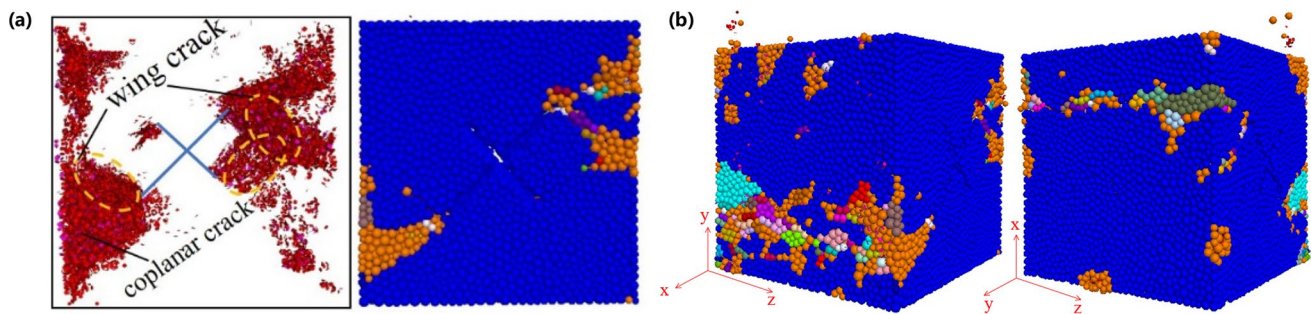


Fig. 17 The final failure state of a specimen under uniaxial compression. **a** Front damage pattern **b** side damage pattern

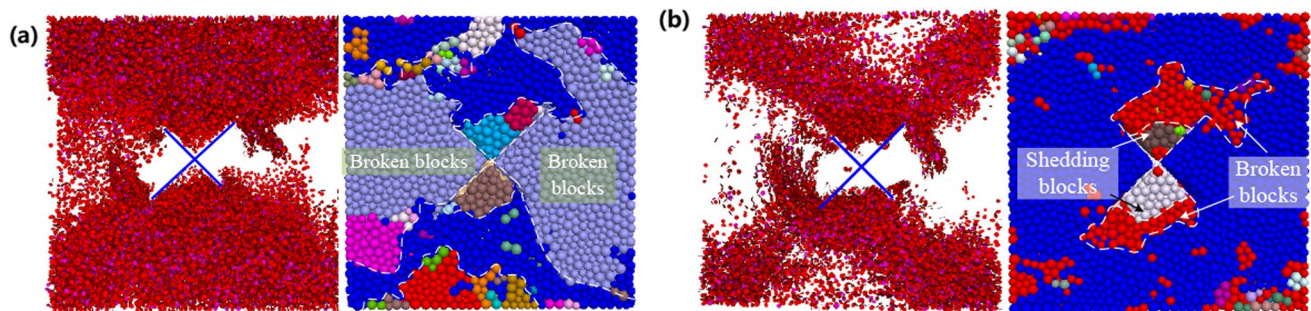


Fig. 18 Final failure patterns of specimens under biaxial and triaxial compression. **a** Biaxial compression **b** triaxial compression

is formed in the sample, which leads to macroscopic damage of the specimen. Under biaxial and triaxial compression, the anti-wing cracks are the main cracks in the crack growth, and both of them penetrate at the tip of primary and secondary joints, but the overall degree of damage to the specimen under triaxial compression is significantly smaller than that under uniaxial and biaxial compression, suggesting that prestressing helps to inhibit the generation of micro-cracks in the specimen, thereby reducing the deformation and damage of the specimen and improving the dynamic strength thereof.

4 Conclusions

The BHPB model was established by the FEM-DEM coupling method, and the results were compared with the laboratory test results, considering the influences of the cross angle, joint persistence ratio, initial stress state, and different modes of crack initiation-propagation in a cross-jointed rock mass under working conditions. The following conclusions can be drawn:

- (1) With the increase in the cross angle α , the peak stress borne by the specimen shows a trend of first decreasing, then increasing, and it is the smallest when $\alpha = 90^\circ$. When $\alpha < 60^\circ$, regardless of the joint persistence ratio η , the dynamic peak stress of the specimen is controlled by the main joints. When $\alpha \geq 60^\circ$, the peak stress decreases with the increase of η , and when $\alpha = 90^\circ$, the peak stress decreases from 169.7 to 152.4 MPa with the increase of η from 0.33 to 1.00, the peak strain significantly reduces to 0.0062.
- (2) Under the initial static load, the initiation and propagation of wing cracks are limited. When $\alpha < 60^\circ$, the crack initiation-propagation of the cross-jointed specimen is mainly controlled by the main joints, and the final fracture surface of the specimen is composed of the main joints and anti-wing cracks; when $\alpha \geq 60^\circ$ or $\eta \geq 0.67$, the interaction is obvious, and the secondary joints have a guiding effect on the propagation of the anti-wing cracks. The primary and secondary joints will be penetrated, and damaged, and multiple fracture surfaces composed of primary and secondary joints, anti-wing cracks and coplanar cracks will be formed.
- (3) The increase in lateral restraint can significantly increase the dynamic peak stress borne by the specimen. its peak stress increases from 76.3 MPa under uniaxial compression to 244.2 MPa (triaxial compression), Under uniaxial compression, the specimen forms a fracture surface composed of primary and secondary joints, wing cracks and coplanar cracks. The degree of damage is greatly reduced.

Limitations It should be mentioned here that the work presented in this study does has a potential limitation. One major issue is that all tests are not repeated based on sufficient samples, and this limiting factor may have some impact on the statistical reliability of the study results.

Acknowledgements The research was financially supported by Open Research Fund of Hubei Key Laboratory of Blasting Engineering HKL-BEF202006) and the National Natural Science Foundation of China (52079102, 52108368).

Author contribution TL: Writing-review and editing, Data curation, Investigation, Visualization. WH: Formal analysis, Data curation, Conceptualization, Funding acquisition. CX: Conceptualization, Methodology, Formal analysis, Funding acquisition. QD: Formal analysis, Data curation, Conceptualization. XL: Writing-review and editing, Data curation. CZ: Data curation, Funding acquisition.

Declarations

Conflict of interest The authors declare that they have no known competing financial interests or personal relationships that could have appeared to influence the work reported in this paper.

Open Access This article is licensed under a Creative Commons Attribution 4.0 International License, which permits use, sharing,

adaptation, distribution and reproduction in any medium or format, as long as you give appropriate credit to the original author(s) and the source, provide a link to the Creative Commons licence, and indicate if changes were made. The images or other third party material in this article are included in the article's Creative Commons licence, unless indicated otherwise in a credit line to the material. If material is not included in the article's Creative Commons licence and your intended use is not permitted by statutory regulation or exceeds the permitted use, you will need to obtain permission directly from the copyright holder. To view a copy of this licence, visit <http://creativecommons.org/licenses/by/4.0/>.

References

- Bahaaddini M, Hagan P, Mitra R, Hebblewhite BK (2016) Numerical study of the mechanical behavior of nonpersistent jointed rock masses. *Int J Geomech* 16(1):04015035
- Cao P, Liu TY, Pu CZ, Lin H (2015) Crack propagation and coalescence of brittle rock-like specimens with pre-existing cracks in compression. *Eng Geol* 187:113–121
- Chang LF, Konietzky H, Frühwirt T (2019) strength anisotropy of rock with crossing joints: results of physical and numerical modeling with gypsum models. *Rock Mech Rock Eng* 52:2293–2317. <https://doi.org/10.1007/s00603-018-1714-8>
- Chen YL, Hao XJ, Xue DJ, Li Z, Ma XR (2023) Creep behavior and permeability evolution of coal pillar dam for underground water reservoir. *Int J Coal Sci Technol* 10(1):11. <https://doi.org/10.1007/s40789-023-00563-y>
- Cundall PA, Strack OD (1979) A discrete numerical model for granular assemblies. *Geotechnique* 29(1):47–65
- Feng F, Chen SJ, Zhao XD, Li DY, Wang XL, Cui JQ (2022) Effects of external dynamic disturbances and structural plane on rock fracturing around deep underground cavern. *Int J Coal Sci Technol* 9(1):15. <https://doi.org/10.1007/s40789-022-00487-z>
- Gong FQ, Li XB, Liu XL (2012a) Preliminary experimental study of characteristics of rock subjected to 3D coupled static and dynamic loads. *China Rock Mech Rock Eng* 30(6):1179–1190
- Gong FQ, Li XB, Liu XL (2012b) Tests for sandstone mechanical properties and failure model under triaxial SHPB loading. *China SHOCK VIB* 31(8):29–32
- He MM, Zhao JR, Deng BY, Zhang ZQ (2022) Effect of layered joints on rockburst in deep tunnels. *Int J Coal Sci Technol* 9(1):21. <https://doi.org/10.1007/s40789-022-00489-x>
- Hu WR, Liu K, Potyondy DO, Zhang QB (2020) 3D continuum-discrete coupled modelling of triaxial Hopkinson bar tests on rock under multiaxial static-dynamic loads. *Int J Rock Mech Min* 134:104448
- Kulatilake PHSW, Malama B, Wang J (2001) Physical and particle flow modeling of jointed rock block behavior under uniaxial loading. *Int J Rock Mech Min* 38(5):641–657
- Li JC, Ma GW (2009) Experimental study of stress wave propagation across a filled rock joint. *Int J Rock Mech Min* 46(3):471–483
- Li XB, Zhou ZL, Ye ZY, Ma CD, Zhao FJ, Zhuo YJ, Hong L (2008) Study of rock mechanical characteristics under coupled static and dynamic loads. *China Rock Mech Rock Eng* 7:1387–1395
- Li XB, Gong FQ, Gao K, Yin SB (2010) Test study of impact failure of rock subjected to one-dimensional coupled static and dynamic loads. *China Rock Mech Rock Eng* 29(2):251–260
- Li YH, Peng JY, Zhang FP, Qiu ZG (2016) Cracking behavior and mechanism of sandstone containing a pre-cut hole under combined static and dynamic loading. *Eng Geol* 213:64–73
- Li XB, Zhou T, Li DY (2018) Dynamic strength and fracturing behavior of single-flawed prismatic marble specimens under impact loading with a split-hopkinson pressure bar. *Rock Mech Rock Eng* 50(1):29–44

- Li DY, Wan QR, Zhu QQ (2020) Experimental study on mechanical properties and failure laws of granite with an artificial flaw under coupled static and dynamic loads. *China Rock Mech Rock Eng* 39(6):1081–1093
- Li DY, Wan QR, Zhu QQ, Hu CW (2021) Experimental study on mechanical properties and failure behaviour of fractured rocks under different loading methods. *J Min Sci* 38(05):1025–1035
- Li JC, Yuan W, Li HB, Zou CJ (2022) Study on dynamic shear deformation behaviors and test methodology of sawtooth-shaped rock joints under impact load. *Int J Rock Mech Min* 158:105210
- Liu QS, Xu J, Liu XW, Jiang JD, Liu B (2015) The role of flaws on crack growth in rock-like material assessed by AE technique. *Int J Fract* 193:99–115
- Liu JM, Sun SR, Yue L, Wei JH, Wu JM (2017) Mechanical and failure characteristics of rock-like material with multiple crossed joint sets under uniaxial compression. *Adv Mech Eng* 9(7):1687814017708710
- Liu XW, Liu QS, Liu B, Zhu YG, Zhang PL (2018) Failure behavior for rocklike material with cross crack under biaxial compression. *J Mater Civ Eng* 31(2):06018025
- Liu K, Zhang QB, Wu G, Li JC, Zhao J (2019) Dynamic mechanical and fracture behaviour of sandstone under multiaxial loads using a triaxial hopkinson bar. *Rock Mech Rock Eng* 52(7):2175–2195
- Liu K, Zhao J, Wu G, Maksimenko A, Haque A, Zhang QB (2020) Dynamic strength and failure modes of sandstone under biaxial compression. *Int J Rock Mech Min* 128:104260
- Liu TT, Xiang C, Zhang C, Li XP, Ding LY, Yuan W (2023) Research on dynamic mechanical properties of rock mass with orthogonal intersecting cracks under two-dimensional static loading. *China Rock Mech Rock Eng*. <https://doi.org/10.13722/j.cnki.jrme.2022.1351>
- Meng FZ, Zhou H, Wang ZQ, Zhang LM, Kong L, Li SJ, Zhang CQ (2016) Experimental study on the prediction of rockburst hazards induced by dynamic structural plane shearing in deeply buried hard rock tunnels. *Int J Rock Mech Min Sci* 86(2016):210–223
- Pan B, Wang XG, Xu ZY, Guo LJ, Li XS (2021) Research on the effect of joint angle on dynamic responses of rock materials. *China Rock Mech Rock Eng* 40(3):566–575
- Shi C, Yang W, Yang J, Chen X (2019) Calibration of micro-scaled mechanical parameters of granite based on a bonded-particle model with 2D particle flow code. *Granul Matter* 21:38. <https://doi.org/10.1007/s10035-019-0889-3>
- Wang HC, Zhao J, Li J, Liu K, Braithwaite CH, Zhang QB (2021) Dynamic mechanical properties and fracturing behaviour of concrete under biaxial compression. *Constr Build Mater* 301:124085
- Weng L, Li XB, Taheri A, Wu QH, Xie XF (2018) Fracture evolution around a cavity in brittle rock under uniaxial compression and coupled static-dynamic loads. *Rock Mech Rock Eng* 51(2):531–545
- Whittaker BN (1988) Analytical and computational methods in engineering rock mechanics, edited by By E. T. Brown Allen and Unwin, London, 1987, No. of pages: 259. *Earthq Eng Struct Dyn* 16:471. <https://doi.org/10.1002/eqe.4290160314>
- Xiao P, Li DY, Zhao GY, Zhu QQ, Liu HX, Zhang CS (2020) Mechanical properties and failure behavior of rock with different flaw inclinations under coupled static and dynamic loads. *J Cent South Univ* 27(10):2945–2958
- Xiong LX, Chen HJ, Geng DX (2020) Uniaxial compression study on mechanical properties of artificial rock specimens with cross-flaws. *Geotech Geol Eng* 39(2):1667–1681
- Xu SL, Shan JF, Zhang L, Zhou LJ, Gao GF, Hu SS, Wang PF (2019) Dynamic compression behaviors of concrete under true triaxial confinement: an experimental technique. *Mech Mater* 140:103220
- Zhang P, Li N, He RL, Xu JG (2006) Mechanism of fracture coalescence between two pre-existing flaws under dynamic loading. *Rock Mech Rock Eng* 2006(06):1210–1217
- Zhou XP, Zhang JZ, Wong LNY (2018) Experimental study on the growth, coalescence and wrapping behaviors of 3D cross-embedded flaws under uniaxial compression. *Rock Mech Rock Eng* 51(5):1379–1400
- Potyondy D (2016) Material-modeling support in PFC [fistPkg21]. Itasca Consulting Group. Inc., Technical Memorandum ICG7766-L, Minneapolis, Minnesota
- Wang W, Wang H, Li DY, Li HM, Liu ZM (2018) Strength and failure characteristics of natural and water-saturated coal specimens under static and dynamic loads. *Shock Vib* 2018
- Wang F, Wang MX, Wang HB, Wang H, Zong Q (2022) Experimental study on the dynamic mechanical properties of a jointed rock mass under impact loading. *Shock Vib* 2022

Publisher's Note Springer Nature remains neutral with regard to jurisdictional claims in published maps and institutional affiliations.